IEEE Access
Multidisciplinary | Rapid Review | Open Access Journal

Received 21 October 2022, accepted 30 October 2022, date of publication 1 November 2022, date of current version 9 November 2022.

*Digital Object Identifier 10.1109/ACCESS.2022.3218892*

RESEARCH ARTICLE

# Concealed Object Detection With Microwave Imaging Using Vivaldi Antennas Utilizing Novel Time-Domain Beamforming Algorithm

**ATHUL O. ASOK, (Graduate Student Member, IEEE), GOKUL NATH S. J., (Member, IEEE), AND SUKOMAL DEY, (Senior Member, IEEE)**

Department of Electrical Engineering, Indian Institute of Technology Palakkad, Palakkad, Kerala 678557, India

Corresponding author: Sukomal Dey (sukomal.iitpkd@gmail.com)

This work was supported in part by the Corporate Social Responsibility, Western India Kinfra Ltd., under Project IITPKD/ICSR/2021/0.05; and in part by the IEEE Antennas and Propagation (AP) Society through the AP-S Fellowship under Grant 2022.

**ABSTRACT** A time-domain novel beamforming algorithm for ultra-wideband (UWB) microwave imaging is furnished in this paper. A monostatic and bistatic antenna setup is utilized to transmit and receive custom UWB pulses. This setup is employed to image various metallic and non–metallic threats attached to a human body. The imaging results demonstrate that the proposed beamforming algorithm allows effective reconstruction of different targets for both monostatic and bistatic cases. An ultra-wideband high gain Antipodal Vivaldi Antenna (AVA) is used as the transducer for the proposed imaging setup. The designed transducer demonstrates measured impedance bandwidth from 660 MHz to 15 GHz (182%) with a peak gain of 15 dBi at 8 GHz. The quality and accuracy of the proposed beamforming algorithm is tested outside the anechoic chamber just to make it more convincing in a real-world dynamic scenario. The result shows that different concealed materials can be detected accurately with the beamforming algorithm. To the best of the authors' knowledge, the proposed algorithm can effectively add up the target responses to obtain a clear and distinct image of the metallic and non-metallic targets.

**INDEX TERMS** Antipodal Vivaldi Antenna (AVA), beamforming algorithm, bistatic, concealed,high gain, human body, metallic, monostatic, non-metallic, novel beamforming algorithm, ultra-wideband (UWB).

## I. INTRODUCTION

The detection of concealed weapons is becoming crucial for the safety of public resources such as airports, sensitive buildings, as well as for public security. X-ray scanning and metal detectors are widely utilized screening procedures in sensitive public spaces such as airports and train stations. These systems, however, have limits when it comes to identifying modern threats such as firearms, blades, and knives, as well as exceedingly lethal weapons composed of a hybrid blend of metal, plastic, and ceramic materials. The negative health effects of X-rays generated by ionization restrict their public adoption. The need to identify modern weapons disguised beneath human clothing without making contact led to the use of microwave imaging systems as a viable contender in such instances.

Microwave imaging is a method capable of determining the presence and dimensions of various objects by using electromagnetic waves at microwave frequency range. Some of the common microwave imaging applications are non-destructive testing [1], moisture detection [2], radar imaging [3] and near-field tomography [4]. The different methodologies to reconstruct the target include qualitative methods [5], quantitative methods [6] and hybrid methods [7]. Synthetic Aperture Radar (SAR) is a widely popular algorithm that can be applied for the detection of targets for security imaging applications. But in the case of SAR algorithm [8], the responses from the entire target area is considered. It gives a good quality image of the target area but, the exact dimensions of the target may not be achieved clearly. Utilizing the responses from the target and as well as

The associate editor coordinating the review of this manuscript and approving it for publication was Qi Luo.

its entire surroundings increases the volume of data storage unit. This affects the complexity and processing time of the image reconstruction procedure. Various beamforming algorithms have also been implemented that demonstrates simple and effective ways to reconstruct the target data. A confocal microwave imaging technique that utilizes the Delay-And-Sum algorithm (DAS) was first proposed [9]. Later, microwave imaging via space-time beamforming [10] was introduced as an improvement over the DAS algorithm. The other emerging image reconstruction algorithms that have been considered are time-reversal [11], generalized likelihood ratio test [12], and multistatic adaptive microwave imaging [13]. Delay multiply and sum algorithm (DMAS) which is a modified version of the DAS algorithm that incorporates pairing multiplication was implemented in [14]. In all these cases, the target is scanned in the horizontal plane. The issue with these methods is that these algorithms are a bit strenuous to apply for security imaging as large number of measured data is required to reconstruct the target.

The walk-through metal detector (WTMD) gates are the most commonly used equipment for security scanning applications. It can detect ferrous items and is best suited for firearm detection. Another way of identifying various concealed targets is to measure the ringing of conducting objects after applying a pulse of electromagnetic radiation-based Late Time response (LTR) [15]. But, these methods cannot identify non-metallic threats such as ceramic knives, plastic guns, powder explosives, and liquids. Millimeter-wave-based 3D imaging methods, which are developed from microwave holography techniques, are also employed to identify concealed weapons and contraband [16]. Terahertz and millimetre [17] wave technologies are limited in their use in the current context due to the high cost of imaging setups. The public has also expressed privacy concerns about the high-resolution 2D images created by both these technologies. These difficulties limit the use of millimetre waves and Terahertz systems in real-time applications, making these aforementioned technologies irrelevant for security applications. There are several weapons with differing dielectric characteristics accessible globally, and present techniques cannot detect those targets.

To address these deficiencies and detect such threats, an Ultra-Wideband (UWB) Antipodal Vivaldi Antenna (AVA) is designed in conjunction with an new image reconstruction algorithm in this work. The UWB antennas having high directivity and broad bandwidth are desirable to obtain a good spatial and axial resolution of the target. The Vivaldi antenna appears to be a good choice for microwave imaging applications because of its wide array of features such as wide bandwidth, narrow beam-width, directive radiation pattern, low cost, low profile, and small size, as discussed in [18], [19], [20], [21], [22], and [23]. Several modifications on AVAs like metamaterial slabs enhanced AVA [24], slotted AVA [25], lens loaded Vivaldi Antenna [26], [27], Artificial Intelligence based Vivaldi Antenna design optimization [28] are reported in the literature. Due to its flexibility in performance enhancement, end-fire radiation pattern and having a planar structure, an AVA is proposed in this work operating in the UWB range (3.1 – 10.6 GHz).

In microwave imaging, the use of UWB results in the generation of high-resolution images due to the high bandwidth spectrum. The UWB unlicensed frequency band contains both low and high-frequency details. The low frequency region gives high depth of penetration whereas the high frequency region gives high resolution. The UWB range consists of both these regions and this makes the devices operating in the UWB range popular in the imaging scenario. Also, successful imaging systems require pre-processing for backscattered signals to remove the unwanted echoes and reflections followed by a well-structured set of procedures to identify a wide range of hidden targets such as metals, liquid, plastics and ceramic.

Due to the above mentioned shortcomings, this work proposes a novel image reconstruction algorithm that is able to effectively detect metallic as well as non-metallic targets with less number of data points and scanning positions. The complete analysis of the proposed algorithm is also provided. Finally, the imaging results after scanning diverse targets like metallic gun, knife, blade, plastic gun, sanitizer bottle, ceramic and powder packet is displayed with both monostatic and bistatic approaches. The analysis of the UWB transducer utilized for scanning these targets is also presented in this paper.

The overall paper is organized as follows: Section II describes the measurement setup of the proposed work, Section III details the general imaging mechanism and clutter removal. Section IV details the proposed imaging algorithm. Also, Section V discusses the antenna utilized for imaging various targets and Section VI elaborates the imaging results. The comparison of the proposed method with the existing SAR algorithm is discussed in Section VII and the salient features of the proposed work is discussed in Section VIII. Finally, the work is concluded in Section IX.

## II. MEASUREMENT SETUP OF THE PROPOSED WORK

In the proposed work, different metallic objects that can cause fatality to a person like a gun, knife and blade are attached to a person in a laboratory setting outside the anechoic chamber to mimic a real-life scenario. Various non–metallic objects like a plastic gun, sanitizer bottle, powder and ceramic are also tested in this work. These objects with their dimensions are shown in Fig. 1. Initially, a single antenna is used for measurement that acts as a transmitter and receiver, forming the monostatic arrangement. Later, an extra copy of the designed antenna is fabricated and placed at a distance of $\lambda/2$ from the former antenna to form the bistatic arrangement. Here, $\lambda$ corresponds to the wavelength at the centre frequency of the operating band. In this work, antenna 1 acts as the transmitter and antenna 2 acts as the receiver. The monostatic and bistatic antenna arrangements are placed over a height-adjustable tripod stand. A schematic of the imaging setup utilized in the propsed work is displayed in Fig. 2, for better clarity.

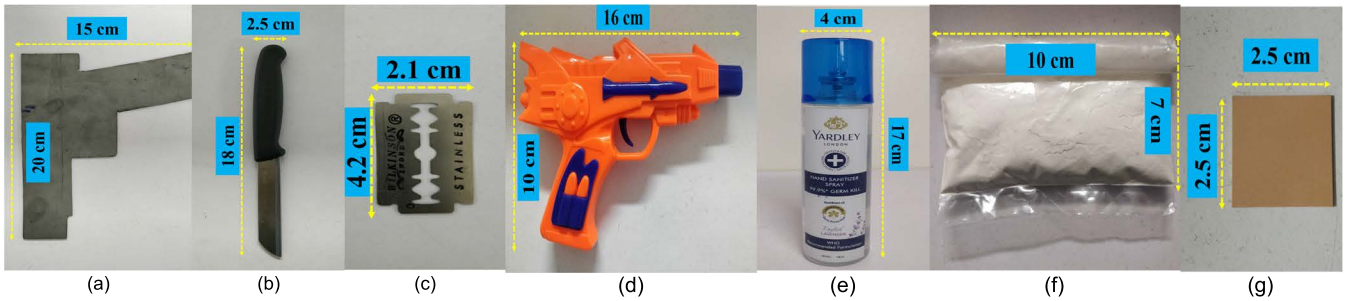


**FIGURE 1.** Different materials under test. (a) gun, (b) knife, (c) blade, (d) plastic gun, (e) sanitizer bottle, (f) powder and (g) ceramic.

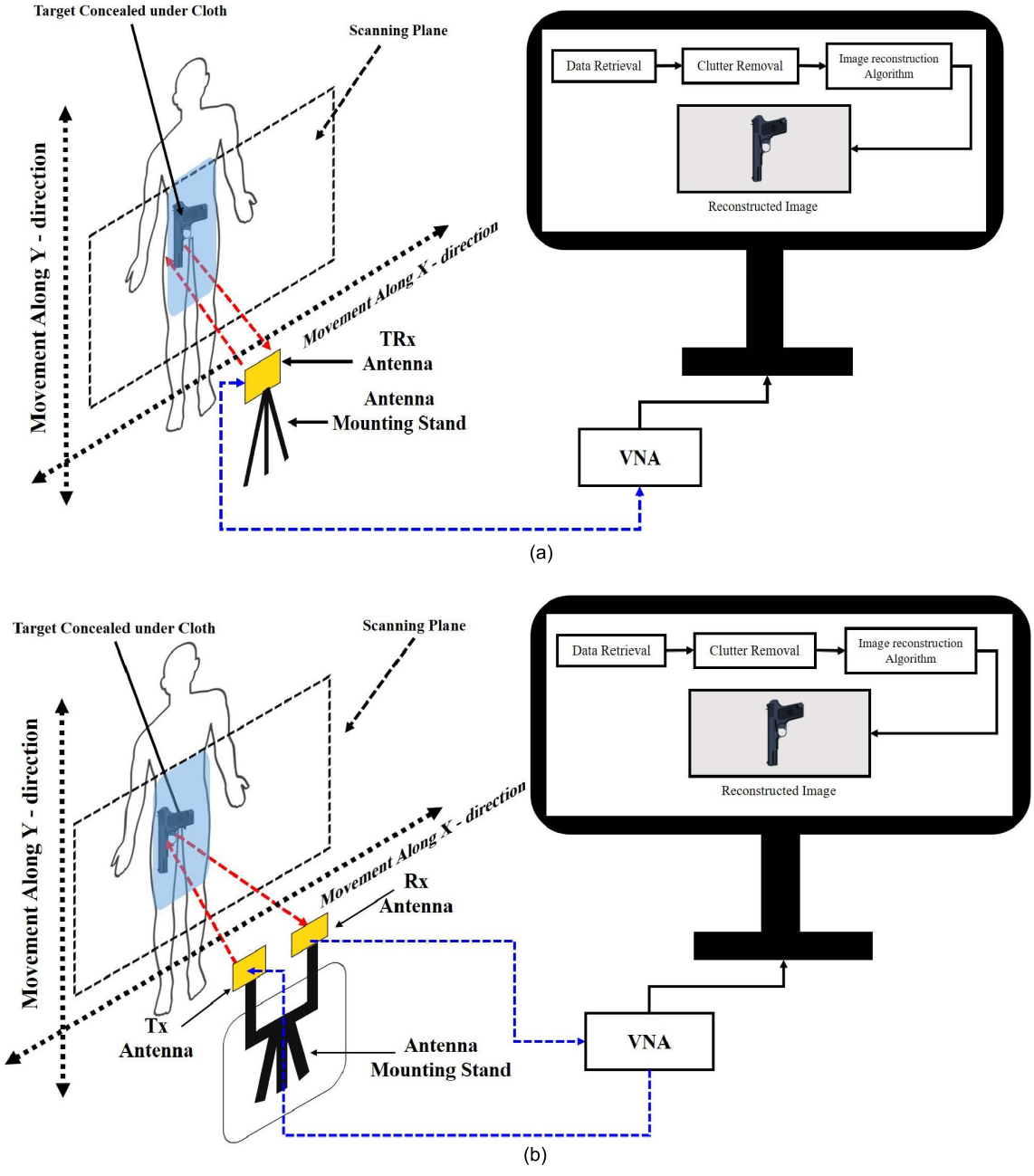


**FIGURE 2.** The schematic of the imaging setup. (a) Monostatic case and (b) bistatic case.

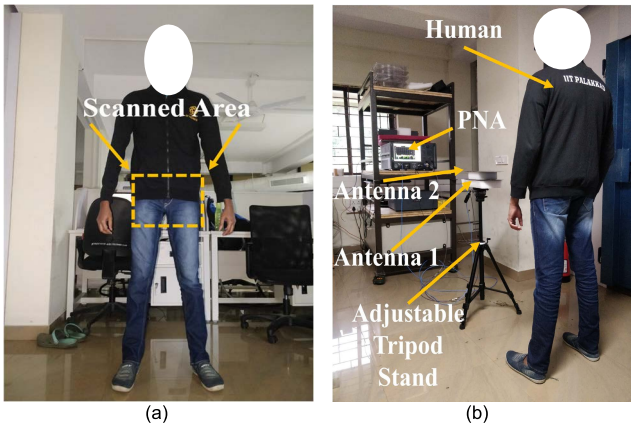


**FIGURE 3.** Measurement setup. (a) concealed human target and (b) complete imaging setup.

In this figure, Fig. 2 (a) displays the complete imaging system and the all the imaging setup parts in the case of monostatic imaging and Fig. 2 (b) displays the same in a bistatic scenario. Initially, the gun replica is placed in the pocket of the person and is used as the target for experiment. This is followed by replacing the gun with a knife and blade as targets. After this, various non–metallic targets are tested. All the materials to be imaged are concealed by a hoodie and jeans before the commencement of the measurement. All the targets to be imaged are placed inside the scanning area depicted clearly in Fig. 3. (a) and the perspective view of the complete imaging setup is displayed in Fig. 3 (b). Note that, the monostatic and bistatic antenna arrangement is placed at a distance of 30 cm from the target for imaging. For clarity, the proposed algorithm was also tested inside the anechoic chamber to detect the hidden targets. The metal gun replica used for testing is made from milled steel of thickness 1.5 mm. The constructed metallic gun is having dimensions similar to that of a real Glock 19. The tripod is physically moved to scan the complete region (11 × 11 locations) surrounding the target. The time-domain data at each location is measured using the time domain response option in the (Keysight) PNA N5224B. The responses at each 11 × 11 locations are tabulated and an appropriate clutter removal procedure and novel image reconstruction algorithm is applied to extract the target response from the tabulated measured data.

## III. IMAGING MECHANISM AND CLUTTER REMOVAL

The microwave imaging system attempts to detect the shape of an object by evaluating its scattered field with efficient antennas, and then applying an effective image reconstruction algorithm to get a clear image of the target. The reflected signals from the target contains the early-time and late-time information. The early-time section mainly consists of the UWB pulse reflections from the hoodie and remnant antenna reverberations, that are classified as clutters. Whereas, the late-time section is composed of human and target responses. The scattering response of a specific target is ideally extracted by measuring the difference of backscattered signals with and without the target. Note that, this is an idealistic approach and this process cannot be done practically due to the complexity in taking the reading at two separate instances for a particular target. Thus, in the proposed work, for clutter removal, the averaging method elaborated in [14] is utilized. After a suitable clutter removal algorithm is applied to the obtained signal, the unwanted recurring responses are filtered out. Following this step, the proposed beamforming algorithm is applied. The proposed algorithm is highly beneficial in the current scenario as this method helps to obtain a distinct image of the target with minimum number of scanning positions. The performance of the proposed algorithm is verified by imaging different metallic and non–metallic targets inside and outside the anechoic chamber. The bandwidth of the designed antenna is exploited to account for good axial resolution of the target and the directional beam of the antenna radiation pattern accounts for the good lateral resolution of the target.

Synthetic Aperture Radar (SAR) is a widely used beamforming method where reflected signals from large number of positions are utilized to produce good quality images of the concealed target. The main disadvantage associated with this approach is that it substantially increases the computational time and the volume of data storage unit. In the case of widely popular DAS approach, the depth plane is considered as opposed to the vertical plane for image reconstruction while detecting the concealed objects. As a result, the DAS method is less significant for concealed object detection purposes. Thus, we need a new method that is computationally efficient, has less scanning time, less data storage size and produces good quality images of the concealed target. The artifact removal method as well as the proposed image reconstruction method used in this work are described in the subsequent sections.

### A. ARTIFACT REMOVAL

In this method, the backscattered signal received at the $(i, j)^{th}$ aperture location is denoted by $b_{ij}[n]$. The reference waveform $R[n]$ that accurately approximates the early time content with negligible late time content is created by averaging all the $M \times N$ (11 × 11) recorded backscattered signals as shown in [9] and [29]. This reference waveform is then utilized for clutter removal by subtracting it from each of the $M \times N$ backscattered signals resulting in $M \times N$ clutter removed signals . The obtained responses contain only the late time information after the clutter removal procedure is applied. This method helps to remove all unwanted clutter obtained in all the antenna stop positions for monostatic and bistatic cases. This method removes clutters up to a reasonable extent with single time scanning of the target area. The clutter removed signal $x_{ij}[n]$, obtained by averaging of all the $M \times N$ backscattered signals is represented by (1),

$$x_{ij}[n] = b_{ij}[n] - R[n] = b_{ij}[n] - \frac{1}{MN}\sum_{i'=1}^{M}\sum_{j'=1}^{N} b_{i'j'}[n], \quad \text{where} \quad i = 1, 2, \ldots\ldots\ldots, M; \quad j = 1, 2, \ldots\ldots\ldots, N. \tag{1}$$

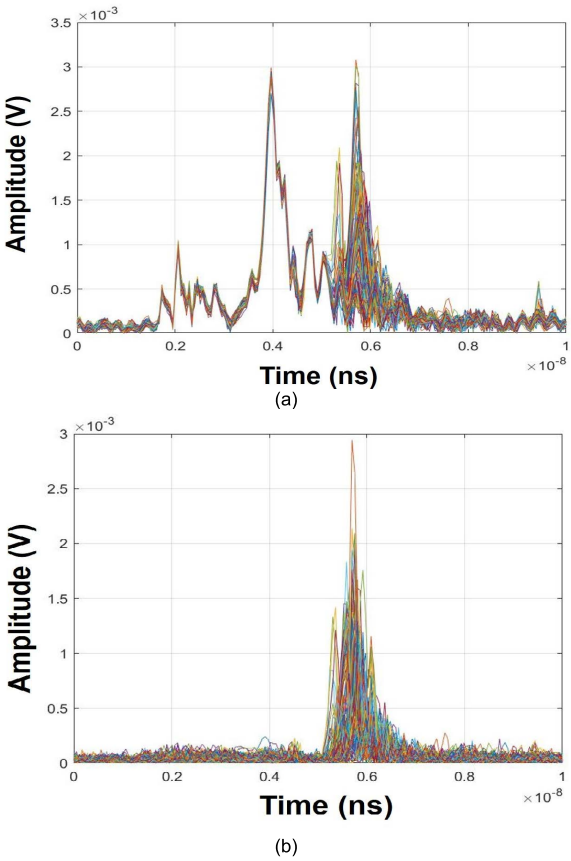


**FIGURE 4.** (a) Received signals (b) clutter removed signals using the averaging technique [14] in a plastic gun.

The received signals and their clutter removed counterparts, while imaging plastic gun is displayed in Fig. 4.

## IV. IMAGING ALGORITHM

In a practical scenario, to detect the concealed targets swiftly, the number of scanned positions should be minimal. In any imaging mechanism, an imaging grid is defined primarily, which is equal to the number of scanned positions of the target. The proposed algorithm assumes an imaging grid of size 11 × 11. Assume the antenna is at position 1 as shown in Fig. 5. From the basic understanding of antennas, it can be inferred that the beam of the antenna diverges as the distance from the antenna increases. This means that the antenna beam impinges on a wide area surrounding the target. In the proposed algorithm, the target plane directly in front of the antenna position is divided into $P_N \times P_N$ (100 × 100) pixels as shown in Fig. 6, and a new imaging grid is formed. Here, the new imaging grid corresponding to antenna location (*11, 11*) ($M = N = 11$) is displayed. After this, the distance from each pixel centre in the new imaging grid to the antenna aperture is calculated using the equation defined by (2),

$$d_{i,j}^{u,v} = \sqrt{(x_i - x_u)^2 + (y_j - y_v)^2 + (z_j - z_w)^2} \tag{2}$$

where $(x_u, y_v, z_w)$ denotes the coordinate positions on the new imaging grid, $(x_i, y_j, z_k)$ represents the antenna position and $d_{i,j}^{u,v}$ denotes the distance from the pixel centre at $(u, v)^{th}$ position in the imaging grid to the $(i, j)^{th}$ aperture location of the antenna. The antenna dimensions $a_n$ cannot be avoided in the calculation of total round-trip distance thus it is added with the previously obtained distance $d_{i,j}^{u,v}$. Thus, the total round-trip distance between the antenna and new imaging grid is estimated based on the expression (3) as,

$$D_{i,j}^{u,v} = 2(d_{i,j}^{u,v} + a_n) \tag{3}$$

After the distance estimation corresponding to the aperture position is done, the time corresponding to the round-trip distance is calculated. The round-trip time is calculated using the expression given in (4).

$$\tau_{i,j}^{u,v} = 2\left(\frac{d_{i,j}^{u,v}}{c}\right) + \frac{2r_c}{c/\sqrt{\varepsilon_{rc}}} + \frac{2a_n}{c/\sqrt{\varepsilon_{ra}}} \tag{4}$$

where, $r_c$ is the thickness of the hoodie (4mm), $a_n$ is the total length of the antenna (356.8 mm), $\varepsilon_{rc}$ (∼2) and $\varepsilon_{ra}$ represents the dielectric constants of cloth and antenna respectively. The received signal is clutter removed to remove the early time responses and other unwanted scatterers. This is performed utilizing the expression (1). Hilbert transform is applied to the clutter removed responses received from each of the antenna stop positions. After this step, envelope detection is done with the help of the expression given in (5).

$$H_{ij}(t) = \left|x_{ij} + j\,\mathcal{H}\left\{x_{ij}\right\}\right| \tag{5}$$

where, $x_{ij}$ represents the signal after the clutter removal operation and $\mathcal{H}\left\{x_{ij}\right\}$ is its Hilbert transform. $H_{ij}$ represents the envelope of the response. After finding the round-trip flight time $\tau_{i,j}^{u,v}$, an optimal magnitude for the corresponding time was calculated using delay compensation. The magnitude extraction using the delay compensation is expressed as (6).

$$y_{ij}(t) = H_{ij}(t - \tau_{i,j}^{u,v}) \tag{6}$$

where, $H_{ij}\left(t - \tau_{i,j}^{u,v}\right)$ locates the magnitude of the signal corresponding to the time delay $\tau_{i,j}^{u,v}$ calculated based on the distance between a particular pixel situated at a co-ordinate location $(x_u, y_v, z_w)$ in the new imaging grid and the antenna. This delay compensation procedure is repeated for $\forall\,(x_u, y_v, z_w) \epsilon P_N \times P_N$ in the new imaging grid corresponding to a particular antenna location $(i, j)$. The magnitude obtained after delay compensation is assigned to their respective pixel locations. This results in the formation of a 2-dimensional image corresponding to a particular antenna position. The representation of new imaging grid positions corresponding to the location of the antenna position is shown in Fig. 7. The antenna at position (1,1) and its imaging sub-grid is shown in Fig. 7(a). Similarly, the new imaging sub-grids corresponding to antenna at positions (2,1), (11,1) and (11,11) are displayed in Fig. 7 (b) – d) respectively. After an image is formed corresponding to a particular antenna position, the antenna is shifted to the next stop position and

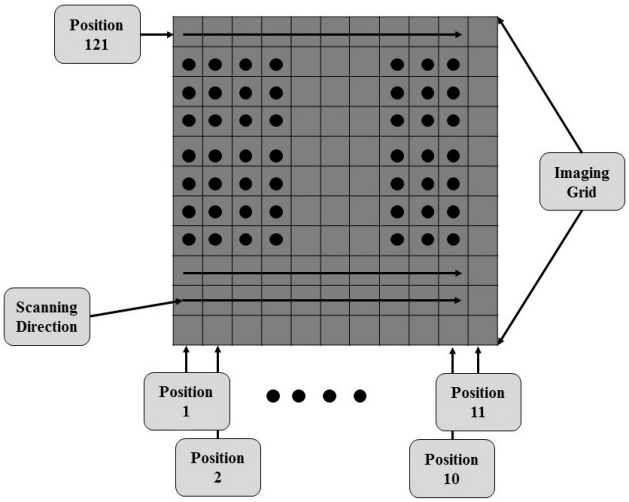


**FIGURE 5.** Imaging grid of the proposed algorithm.

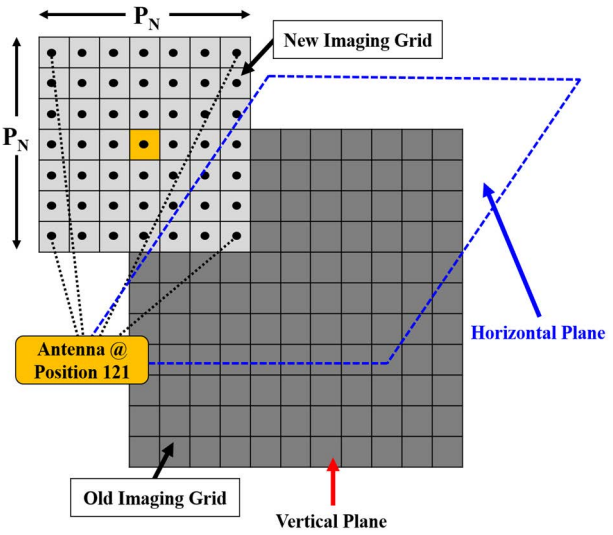


**FIGURE 6.** Schematic of the imaging planes.

the same procedures were repeated to create an image with respect to the next antenna scanning position.

Let $Im_{i,j}$ corresponds to the image formed by the antenna located at the $(i, j)^{th}$ aperture position. To reduce the effect of radial spread, the image is normalized by applying the equations given in (7) - (8).

$$N = max[Im_{i,j}(u, v)] \tag{7}$$

$$Im_{n(i,j)} = Im_{i,j}/N \tag{8}$$

where $(u, v)$ denote the pixel index corresponding to the maximum intensity, $N$ is the maximum intensity of the pixel in the image $Im_{i,j}$ and $Im_{n(i,j)}$ denotes the normalized image corresponding to antenna location $(i, j)$.The procedure is repeated $\forall Im_{i,j}$ where $1 \leq i \leq M$ and $1 \leq j \leq N$ where $M = N = 121$. All the images $Im_{n(i,j)}$ obtained corresponding to each antenna movement is summed up to obtain the desired reconstructed image $Im$, which can be modelled based on the equation given by (9).

$$Im = \sum_{i=1}^{121} \sum_{j=1}^{121} Im_{n(i,j)} \tag{9}$$

The image reconstruction process is represented in the form of a flow chart for better clarity, as shown in Fig. 8.

## V. ANTENNA DESIGN

The different design stages of the antenna utilized for imaging, leading up to the final structure is displayed in Fig 9. Initially in Design A, the flare structure is designed by considering a quarter ellipse in the simulator. The major and minor axis of the ellipse is given by $a$ and $b$, respectively. Patch of dimension $W_G \times L_F$ is etched out initially from the quarter ellipse, followed by another patch of dimension $L_H \times W_H$. After this step, a small triangular portion of the flare is also etched out. The obtained flare edge is extended further inwards by attaching a spline to the ellipse edge. This gives the complete flare design. Following this step, similar shape is made on the backside of the substrate to obtain the complete antipodal structure. A rectangular ground of dimensions $L_I \times W_I$ is also inserted on the rear side.

Design B, as displayed in Fig 9. (b), extends the flare region of the antenna by introducing semicircular sections on the sides of the flares. Three semicircular sections on the left side of the flare and another one on the bottom with their dimensions optimized in the simulator are attached. The designed antenna is fed by a microstrip line having a width labeled $W_F = 4.2$ mm to match the 50 Ω port impedance.

Later, in Design C, semicircular corrugations are made throughout the edges on the modified flares by etching out circles of radius $(R_C)$ 6.6 mm from the outer edges of the flares.16 rectangular slots of dimensions $L_C \times W_C$ mm$^2$ are also etched out from the flare structure, as shown in Fig 9. (c). The corrugations increase the surface currents at the edges of the flares. This expands the operating frequency as well as increases the gain at low-frequency regions.

Finally, the AVA substrate is extended in Design D in a triangular fashion to form the dielectric lens as shown in Fig. 9.(d). The dielectric lens guides the diverging radiation towards the end-fire direction as well as increases the gain at high frequency regions. The entire structure is designed on a Taconic CER substrate with a dielectric constant of 3.2, loss tangent of 0.003 and thickness of 1.14 mm. Fig. 10 (a) and Fig 10 (b) shows the fabricated AVA, front and back, respectively. Fig. 11 illustrates the simulated return loss plot of the proposed AVA at different design stages. It can be noted that for the designed antenna (Design D), the complete region from 660 MHz to 15 GHz is under −10 dB, which furnishes a considerable bandwidth in the UWB range. The low frequency section of the simulated return loss is separately shown in the same figure for better understanding of the antenna performance. The simulated gain performance at different stages in the design is also plotted and displayed in Fig. 12. The measured return loss is plotted and compared with the final design stage and is displayed in Fig. 13.

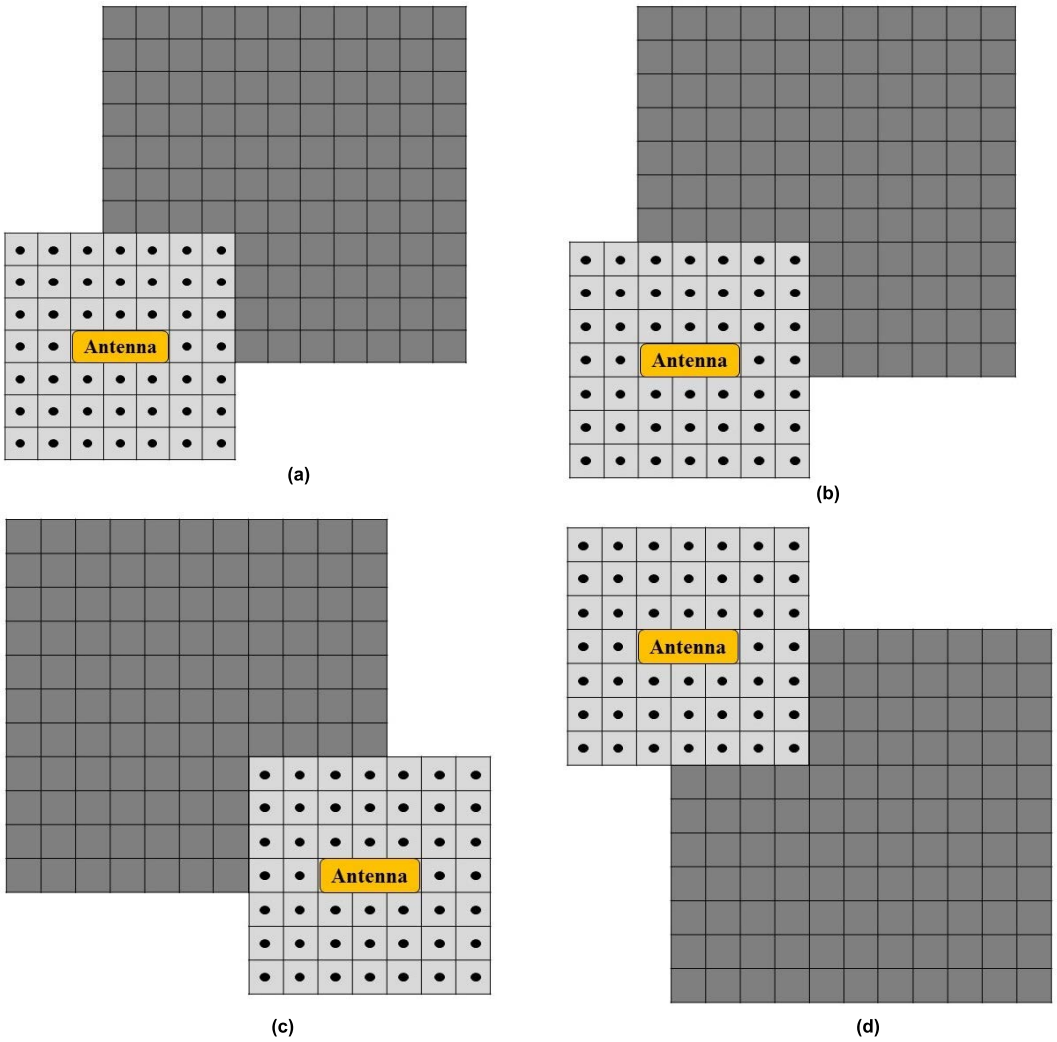


**FIGURE 7.** The new grid corresponding to different antenna positions. (a) Antenna at position (1, 1) (b) Antenna at position (2, 1) (c) Antenna at position (11, 1) and (d) Antenna at position (11, 11).

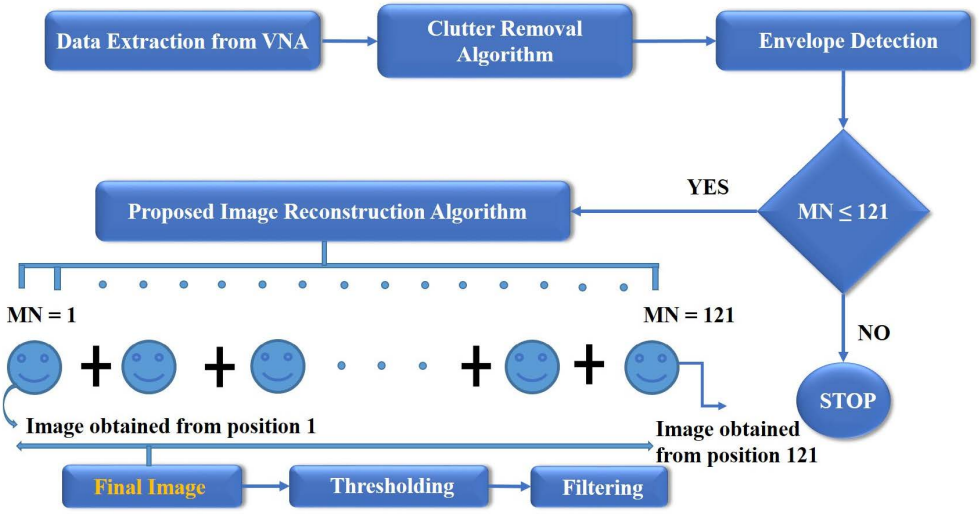


**FIGURE 8.** Flow chart of the proposed imaging methodology.

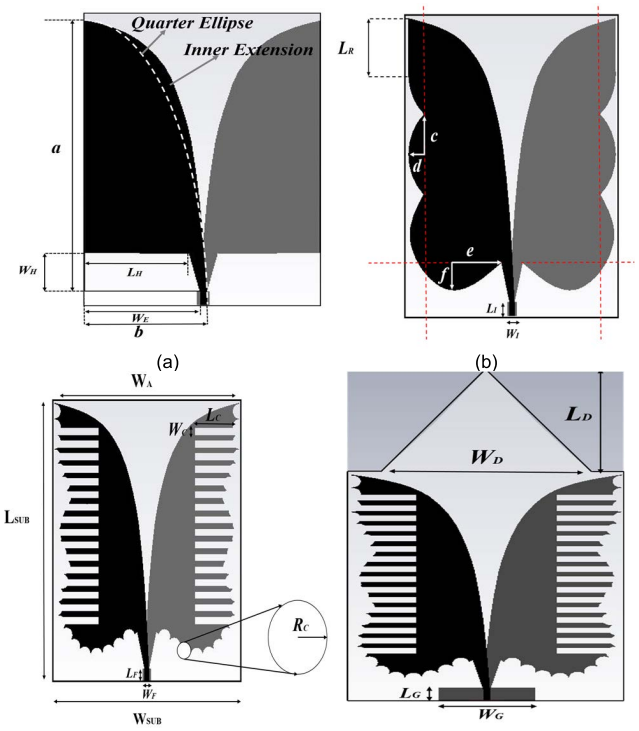


**FIGURE 9.** Different design stages of the proposed antenna leading up to the final structure where (a) Design A, (b) Design B, (c) Design C and (d) Design D.

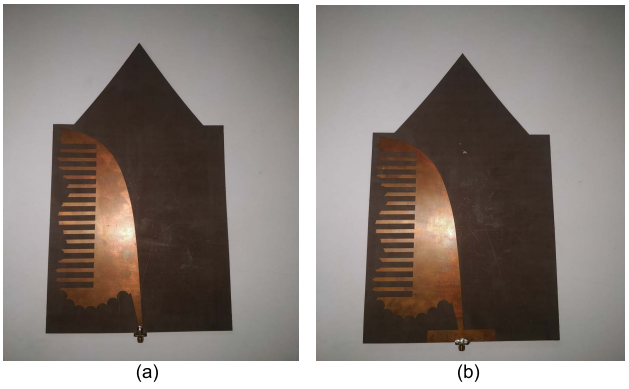


**FIGURE 10.** Fabricated photographs of the AVA (a) Front and (b) Back.

The measured gain versus frequency is also plotted and compared with the simulation performance as displayed in Fig. 14. There is a good harmony between the simulated and measured results with few mismatches. This deviation is mostly attributed to the fabrication tolerances and additional losses from the RF connector. The antenna achieves a peak gain of 15 dBi at 8 GHz. The gain of the antenna is measured using the three-antenna method. Good agreements between simulated versus measured results were obtained up to a reasonable extent. The surface current distribution of the antenna is observed to find the radiating regions of the antenna at specific frequencies, and is displayed in Fig. 15.

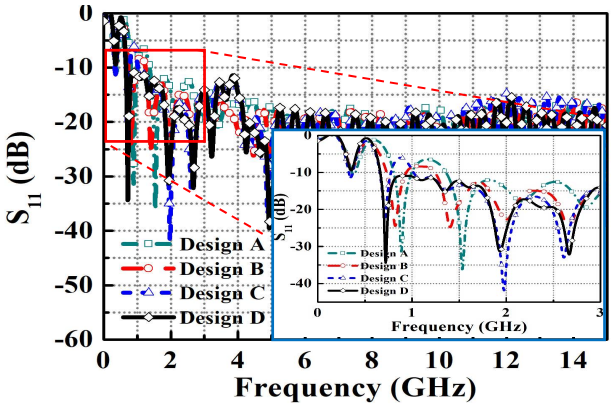


**FIGURE 11.** The simulated return loss at different design stages. Inset shows matching at low frequencies.

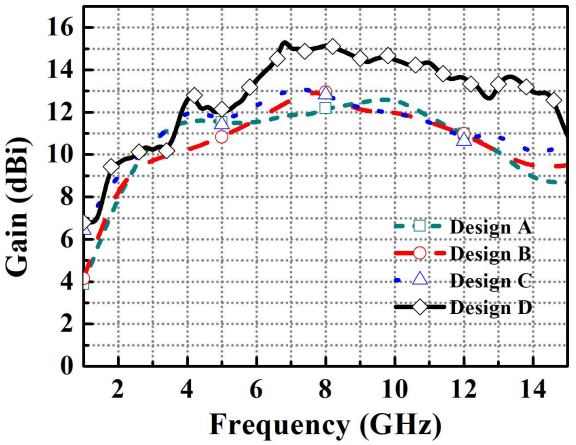


**FIGURE 12.** Simulated gain of the AVA at different stages.

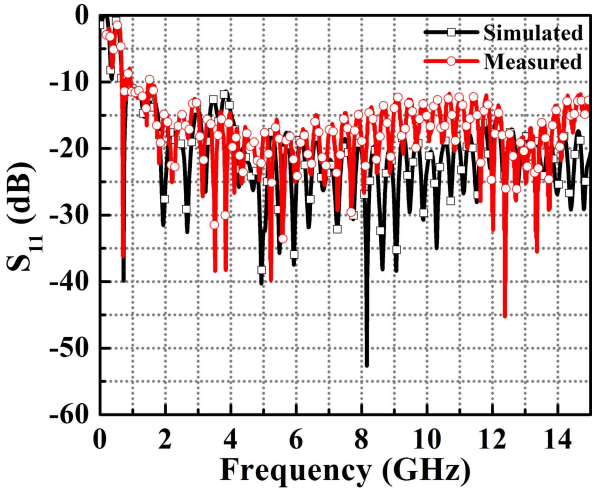


**FIGURE 13.** Simulated versus measured matching ($S_{11}$) responses of the designed AVA.

Fig. 15 (a) – (d) displays the surface currents at 4 GHz, 6 GHz, 8 GHz and 10 GHz, respectively. Fig. 16 (a) displays the antenna measurement setup inside the anechoic chamber and Fig. 16 (b) displays the magnified view of antenna inside

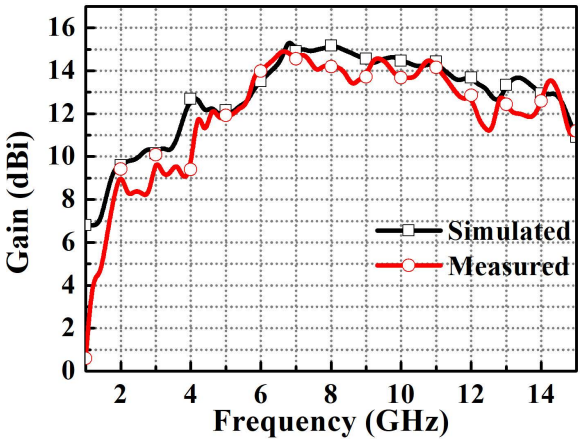


**FIGURE 14.** Simulated versus a measured gain of the designed AVA.

**TABLE 1.** Proposed AVA design parameters.

| $L_{SUB}$ | $W_{SUB}$ | $W_A$ | $L_F$ | $W_F$ | $R_C$ |
|---|---|---|---|---|---|
| 246.4 | 193.2 | 193.2 | 11.12 | 4.2 | 6.8 |
| $L_C$ | $W_C$ | $L_G$ | $W_G$ | $L_D$ | $W_D$ |
| 50 | 6.6 | 13.3 | 67.2 | 110.4 | 147 |
| $a$ | $b$ | $c$ | $d$ | $e$ | $f$ |
| 240 | 82 | 32.85 | 14 | 37.85 | 22 |
| $L_H$ | $W_H$ | $L_I$ | $W_I$ | $W_E$ | $L_R$ |
| 70.5 | 44 | 11.12 | 8.4 | 93 | 41.7 |

All dimensions are in 'mm'

the anechoic chamber. At the transmitting section, a broadband ridged horn antenna is used. The designed antenna whose radiation characteristics is to be determined is placed at the receiving end as displayed clearly in the figure. The antenna is mounted on a movable positioner system which has rotating features in three independent planes to fix its polarization and line of sight alignment with respect to the transmitting horn. Distance between the transmitting horn and the proposed antenna is fixed at 1 meter which satisfies the far-field condition of distance greater than $2D^2/\lambda$. During the experiment inside the anechoic chamber, power to the transmitting horn antenna is kept as 10 dBm. Figs. 17 - 18 shows measured and simulated E-plane and H-plane radiation patterns of the antenna at 2 and 12 GHz, respectively. All the design parameters of the AVA are listed in Table 1 for completeness. The designed antenna is also compared with similar AVAs operating in the low frequency region and is tabulated in Table 2. It can be observed that the designed antenna outperforms other structures in several metrics. A preliminary version of this antenna is reported in [30]. The differences of this fabricated antenna with the antenna reported in [30], are as follows;

**(1)** The dimensions of the proposed antenna are different as compared to the antenna dimensions presented in [30].

**(2)** The design stages of the proposed antenna are also different as compared to the design stages presented in [30].

**(3)** In [30], the antenna was designed on an FR4 substrate of dielectric constant 4.4, loss tangent 0.02 and thickness 1 mm. The antenna also had a tooth-shaped dielectric director made up of Taconic substrate of dielectric constant 10. The proposed structure is entirely designed on the Taconic CER substrate with a dielectric constant of 3.2 and a loss tangent of 0.003 with a thickness of 1.14 mm. In this model, the substrate is extended in a triangular fashion from the antenna mouth opening to form the dielectric lens.

**(4)** In [30], the antenna obtained a peak gain of 11.2 dBi at 6 GHz and the operating range was from 1.9 to 14 GHz. whereas, the fabricated antenna attains a peak gain of 15 dBi at 8 GHz with an operating range from 0.66 - 14 GHz.

Due to the high depth of penetration as well as its wide operating region, the proposed antenna is used for imaging. The structure is fabricated using Monolithic Microwave Integrated Circuit (MMIC) technology and later tested using (Keysight) N5224B Performance Network Analyzer (PNA).

## VI. IMAGING RESULTS

### A. IMAGING OF METALLIC TARGETS

The proposed algorithm is tested outside an anechoic chamber just to mimic the real-life scenarios. Fig. 19 (a) – (d) describes the monostatic results for the metallic gun, knife, blade and combination of all. The bistatic results for individual objects, and with all of them combined are also displayed in Fig. 20 (a) – (d). All the objects are clearly marked in the reconstructed images. Result shows that the bistatic images produce stronger responses than the monostatic case. Note that, the response of the jeans button is clearly eliminated in Fig. 20 (a) and (b). This is because the knife and gun are positioned in such a way that it masks the button. The button is also not visible during blade measurement for both the monostatic and bistatic cases. It is mostly due to fact that the blade and button are at different depths in the bistatic case as well as monostatic case, as shown in Fig. 20. The vertical plane is considered at the blade location for both these cases. The handle section of the knife is not visible in Fig. 19 (d) and Fig. 20 (d), as this is masked by the reflections from the surface of the gun. The intensity of hot points on the reconstructed images obtained from the objects decreased after normalization. It also lead to slight improvement in the quality of the reconstructed images. Note that, the dimensions of the metallic gun, knife and blade are nearly similar to their original dimensions after imaging, as observed from the reconstructed images.

### B. IMAGING OF NON-METALLIC TARGETS

After successful image reconstruction of metallic threats, the proposed methodology is verified with non-metallic targets in a laboratory environment outside the anechoic chamber. The plastic targets are concealed by person's t-shirt and pants while scanning. Note that, the scanning area was kept same as that of the previous targets. Fig. 21 (a) – (d) describes the monostatic results for the plastic gun, sanitizer bottle, powder and ceramic object. The presence of all the targets are clearly detected with the proposed algorithm. Fig. 22 (a) – (d) show the reconstructed images of the same objects with the bistatic

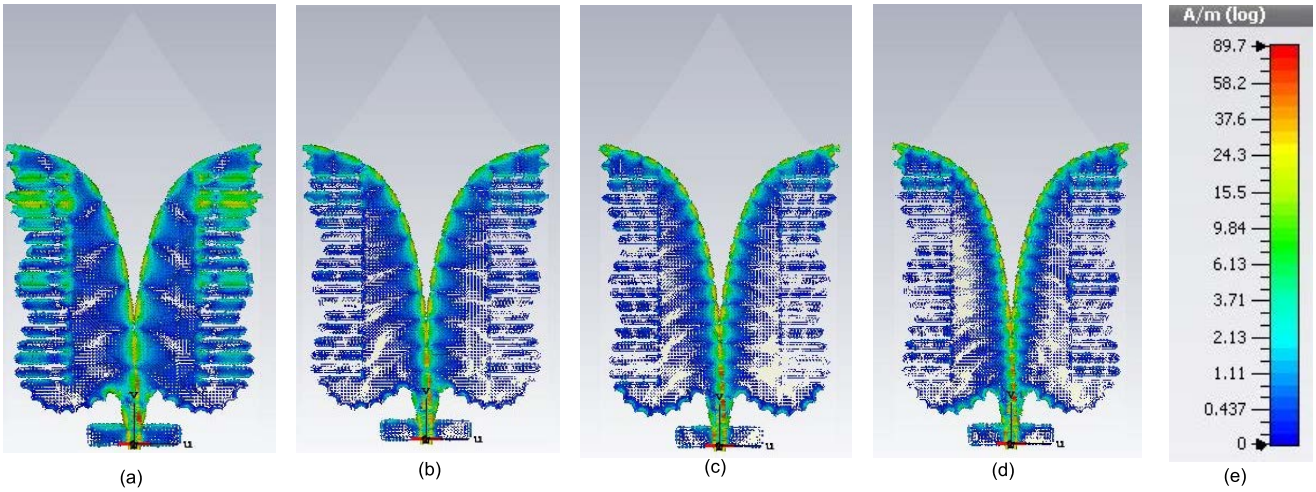


**FIGURE 15.** Surafce current distribution of the designed antenna at (a) 4 GHz, (b) 6 GHz, (c) 8 GHz and (d) 10 GHz. (e) scaling display.

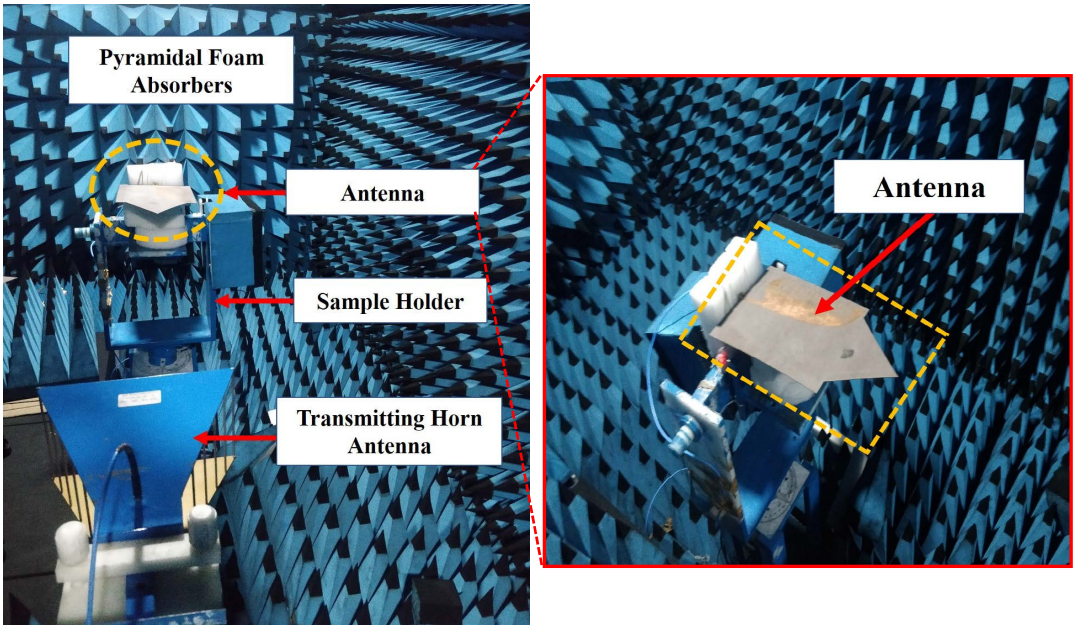


**FIGURE 16.** Measurement setup inside the anechoic chamber, inset shows magnified antenna view inside the anechoic chamber.

**TABLE 2.** Comparison of the designed AVA with similar works in literature.

| References | Return Loss (dB) | -10 dB impedance Bandwidth (%) | Maximum Gain (dBi) (With Lens) | Gain (dBi) (Without Lens) | -3dB Gain Bandwidth | -3dB Gain bandwidth (%) |
|---|---|---|---|---|---|---|
| [24] | 1.5 - 8 | 136.84 | 16.4 | Around 13 | 5 - 8 | 46.15 |
| [25] | 0.8 - 6 | 152.94 | 11 | Nil | 1.5 - 6 | 120 |
| [26] | 1.76 - 10 | 140.13 | 15.83 | Nil | Nil | Nil |
| [27] | 1 - 12 | 169.2 | 10 | 8 | 2 - 10 | 133.3 |
| [28] | 2 - 12 | 142.85 | 11.8 | 6 | 2 – 11.8 | 142 |
| **This Work** | **0.66 - 14** | **182** | **15** | **13.1** | **3.8 - 14** | **114.6** |

method. Note that, the bistatic results display the contours of the plastic targets more clearly as compared to their monostatic counterparts. This is due to the fact that in the case of the monostatic responses, the reflected signals from the target is masked by the reflection from the antenna. The dimensions of the plastic gun with its irregular edges are detected with utmost accuracy. A sanitizer bottle with sanitizer (95% Ethyl Alcohol) is detected clearly with the same dimension as that

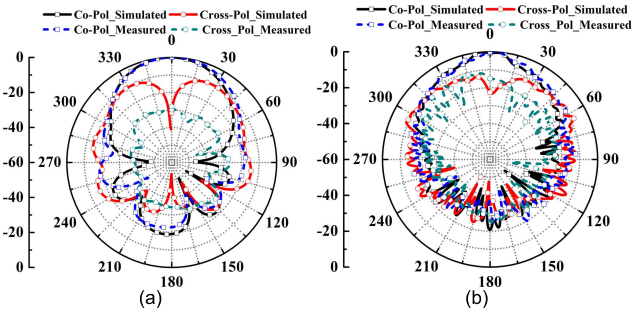


**FIGURE 17.** Measured versus simulated E-plane radiation pattern of the AVA at (a) 2 GHz and (b) 12 GHz.

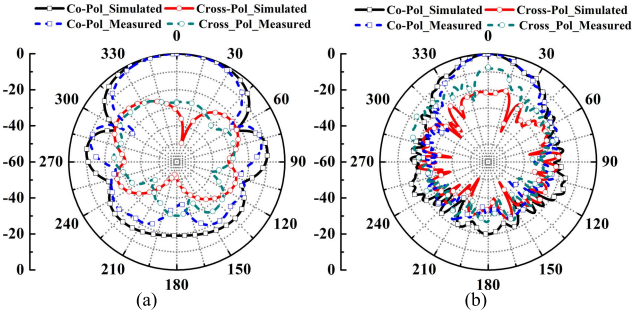


**FIGURE 18.** Measured versus simulated H-plane radiation pattern of the AVA at (a) 2 GHz and (b) 12 GHz.

of the original bottle. Talcum powder was taken in a small packet and that too was detected. The algorithm was finally tested on a ceramic object and the result is also satisfactory.

All these measurements ensure the quality of the proposed method and its usefulness in the detections of any metallic and non–metallic threats. The scanned area is 30 × 30 $cm^2$ and it is constant for all the objects. The distance between the neighboring positions is 3cm. Total 11 × 11 positions were utilized in scanning the target area. There is a relationship between the grid dimension and the dimension of the scanned area. The scanned area is kept fixed throughout the entire process of data acquisition. The sub-grid dimension is varied depending upon the antenna radiation pattern performance. As the radiation pattern becomes more directional, the sub-grid dimension becomes smaller. Similarly, as the radiation pattern becomes more diverging the sub-grid dimension is increased to incorporate all the diverging beam reflections. The time needed for the algorithm to evaluate the data is 11.62 sec with intel i3 Dell Vostro laptop having 8 GB RAM.

## VII. COMPARISON WITH SAR ALGORITHM

To further check the utility of the proposed algorithm, the method is compared with the widely used SAR algorithms reported in [17], [31], [32], [33], [34], [35], and [36]. The image reconstructed with all the metallic targets attached to the human, measured using the bistatic approach, displayed in Fig. 20.(d) is compared with the widely used 2D - SAR algorithm. It is found that the proposed method outperforms the existing SAR approach as displayed in Fig. 23. Previously reported works in [17], [31], [32], and [33] dealt with higher number of scanning positions and hence they are time – consuming in nature. The processing time of the proposed method is considerably less due to fewer scanning aperture

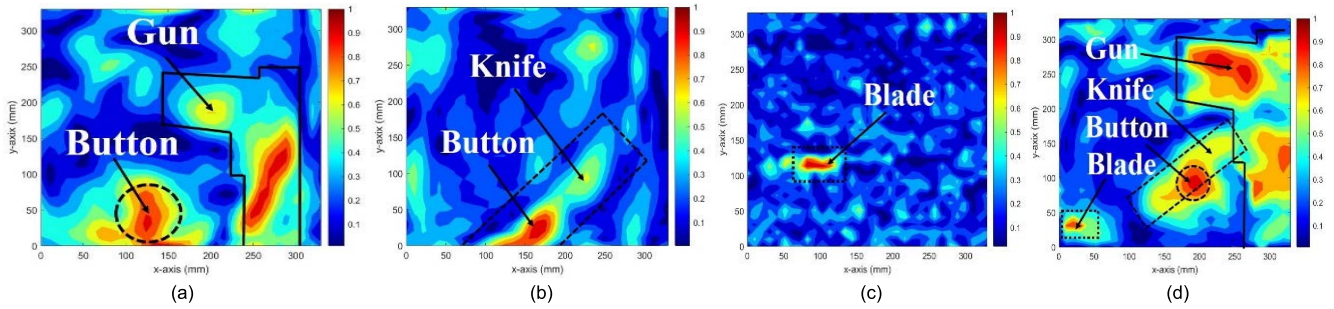


**FIGURE 19.** Monostatic Imaging results of (a) gun, (b) knife, (c) blade and (d) all.

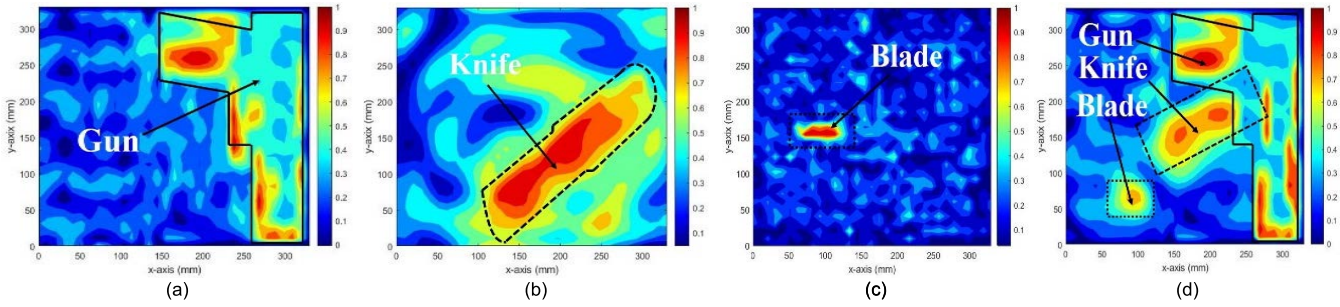


**FIGURE 20.** Bistatic Imaging results for (a) gun, (b) knife, (c) blade and (d) all.

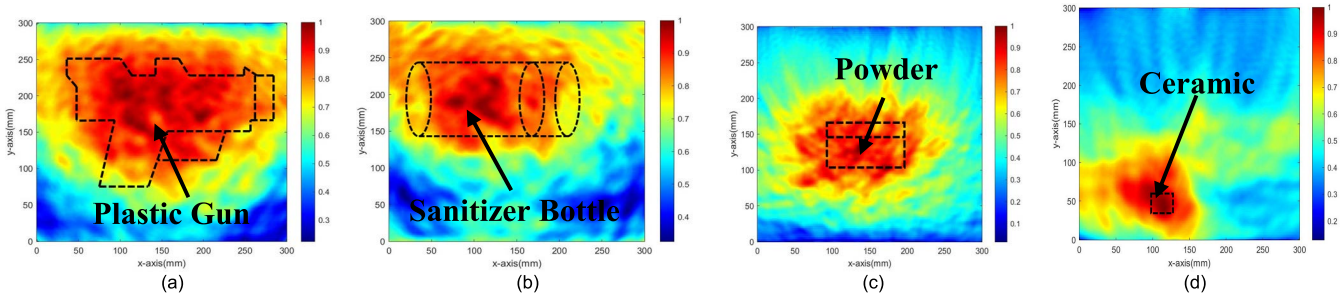


**FIGURE 21.** Monostatic Imaging results of (a) plastic gun, (b) sanitiser bottle, (c) powder and (d) ceramic.

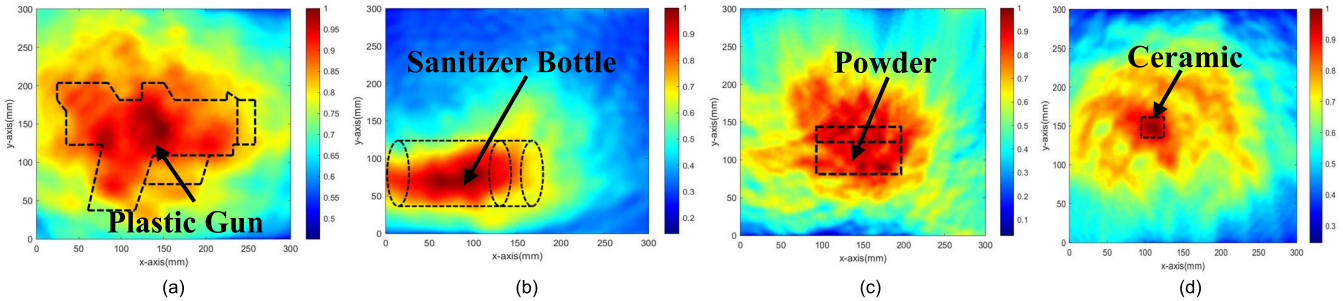


**FIGURE 22.** Bistatic Imaging results of (a) plastic gun, (b) sanitiser bottle, (c) powder and (d) ceramic.

positions. A common imaging approach is to use antenna arrays to cover larger areas. But this involves complex fabrication and several backend designs. These compliactions are resolved by the proposed work.

The comparison of the proposed method with recently reported works on concealed object detection is tabulated in Table 3, for better clarity. In the opinion of the authors, the proposed algorithm effectively imaged a variety of concealed targets clearly, with lesser number of scanning points in monostatic and bistatic arrangements, as compared with other methods reported in [17], [31], [32], [33], [34], [35], and [36]. In the proposed algorithm, smoothness of the reconstructed images are adjusted by increasing the density of the pixel grid. As the sub grid becomes larger, more reflections will be considered for image reconstruction. Please note that the output signal from the PNA is a continuous wave signal, that is utilized for image reconstruction in the proposed work.

## VIII. SALIENT FEATUTES OF THE PROPOSED METHOD

The Salient features of the proposed algorithm are as follows;

**(1)** The proposed method achieves a good quality image of the hidden target using the data obtained from lesser number of scanning positions of the scanned area.

**(2)** The proposed algorithm scans the vertical plane (Plane of the target) in small sub-sections and forms an image corresponding to each sub-section. The image addition of all the images from each sub-section gives the image of the concealed target corresponding to a particular scanned area. The concept of image addition is integrated with the image reconstruction method to clearly detect the target.

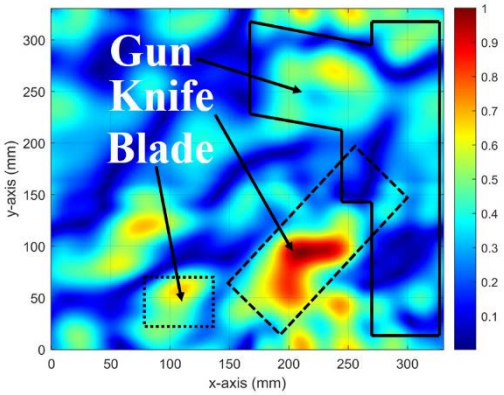


**FIGURE 23.** Reconstructed images of all the metallic targets together with bistatic approach using the conventional SAR method.

**(3)** The run time of the proposed algorithm is less when compared with the other state-of-the-art designs, as the back projection in the proposed algorithm is applied only to a smaller sub-grid with respect to a particular antenna position.

**(4)** The response from each pixel located farther from the main lobe is ignored in the proposed algorithm due to lower intensity levels of the reflected signals. This results in lower complexity in the image reconstruction process and reduces the processing time of the algorithm significantly.

**(5)** In the widely used DAS process, the horizontal plane is employed to identify hidden targets. Since the scanning plane of DAS is unsuitable for identifying concealed targets in the vertical plane, it is generally not used for security imaging applications.

**TABLE 3. Comparison of the proposed method with other reported works.**

| Ref, Year | Antenna | Frequency (GHz) | Elements and scanned position | Beamforming Algorithm | Application |
|---|---|---|---|---|---|
| [31], 2016 | Miniaturized AVA | UWB | 2 Antenna Elements<br>1000 × 500 Pixels | SAR | SAGD Monitoring |
| [33], 2011 | AVA | 2.8 – 19.5 | 12 Antenna Elements | SAR | Concealed object detection |
| [32], 2015 | Horn Antenna | 2.2 - 18 | 2 Antenna Elements<br>800 × 1300 scanned positions | SAR | Imaging Oil Well Perforations |
| [33], 2018 | Vivaldi Antenna | UWB | 2 Elements | SAR | Imaging Anomalies on Metal Pipe |
| [34], 2020 | Vivaldi Antenna | UWB | Multistatic Imaging | CSAR | Imaging Oil and Gas pipeline Cross-section |
| [35], 2021 | RF Sensor | 8 - 12 | Monostatic | SAR | Imaging of Layered Media |
| [36], 2020 | Not Given | UWB | Not Given | SAR | See through wall Applications |
| **This Work** | **AVA** | **0.66 – 14** | **1, 2 Antenna Elements<br>11 × 11 scanned positions** | **Proposed Algorithm** | **Concealed object detection** |

**(6)** As compared to the existing SAR algorithm that reconstructs the image using backscattered signals from a wide area, the proposed algorithm reconstructs the concealed target using the backscattered signals received only from the small region in front of the transducer where most of the radiation impinges. This is done to obtain edges of the concealed target clearly.

To the best of the authors' knowledge, the proposed algorithm is computationally efficient, takes a smaller number of scanning positions with less scanning time and has the capability to detect metallic and non-metallic threats up to a reasonable extent.

## IX. CONCLUSION

In this work, a highly effective and efficient time-domain imaging algorithm is presented for the detection of concealed objects. The introduced algorithm is capable of clearly locating the threats with a minimum number of scanning points ($11 \times 11$) of the concealed target surface. The proposed algorithm reconstructs smaller sections of the target surface from the radiation impinging area and finally superimposes all the images formed corresponding to the 121 scanning locations to get a distinct image of the concealed target. An AVA is used as the transducer to check the utility of the proposed algorithm inside and outside of the anechoic chamber. The utilized AVA has a peak gain of $\sim$15 dBi at 8 GHz and good impedance matching ($>$10 dB) over 660 MHz – 14 GHz (182%). All the design parameters as well as the performace parameters of the antenna is also discussed in the proposed work. The proposed algorithm is extensively tested to detect different metallic (gun replica, knife, blade) and non–metallic (plastic gun, sanitizer bottle, powder and ceramic) threats. In all the cases, satisfactory images of the concealed targets are obtained with appropriate dimensions. It demonstrates the validity, utility and efficiency of the proposed image reconstruction method for security imaging. In the opinion of the authors, the proposed algorithm can be used for biomedical imaging and will be validated in the future.

## ACKNOWLEDGMENT

The authors are grateful to the IEEE AP Society.

## REFERENCES

[1] M. J. Akhtar, *Microwave Imaging*. Berlin, Germany: VDM Verlag, 2008.
[2] P. Mehta, K. Chand, D. Narayanswamy, D. G. Beetner, R. Zoughi, and W. V. Stoecker, "Microwave reflectometry as a novel diagnostic tool for detection of skin cancers," *IEEE Trans. Instrum. Meas.*, vol. 55, no. 4, pp. 1309–1316, Aug. 2006.
[3] F. Viani, P. Rocca, G. Oliveri, D. Trinchero, and A. Massa, "Localization, tracking, and imaging of targets in wireless sensor networks: An invited review," *Radio Sci.*, vol. 46, no. 5, pp. 1–12, Oct. 2011.
[4] M. D. Hossain and A. S. Mohan, "Coherent time-reversal microwave imaging for the detection and localization of breast tissue malignancies," *Radio Sci.*, vol. 50, no. 2, pp. 87–98, Feb. 2015.
[5] M. Pastorino, *Microwave Imaging*. Hoboken, NJ, USA: Wiley, 2010.
[6] D. Colton, H. Haddar, and M. Piana, "The linear sampling method in inverse electromagnetic scattering theory," *Inverse Problems*, vol. 19, no. 6, pp. S105–S137, Dec. 2003.
[7] R. Eskandari and M. R. Eskandari, "Microwave imaging of two-dimensional objects using an enhancement method," *J. Electromagn. Waves Appl.*, vol. 29, pp. 0920–5071, Nov. 2015.
[8] P. T. Gough and B. R. Hunt, "Synthetic aperture radar imaging reconstruction algorithms designed for subsurface imaging," in *Proc. Int. Geosci. Remote Sens. Symp.*, Singapore, May 1997, pp. 1588–1590.
[9] X. Li and S. C. Hagness, "A confocal microwave imaging algorithm for breast cancer detection," *IEEE Microw. Wireless Compon. Lett.*, vol. 11, no. 3, pp. 130–132, Mar. 2001.
[10] E. J. Bond, X. Li, S. C. Hagness, and B. D. Van Veen, "Microwave imaging via space-time beamforming for early detection of breast cancer," *IEEE Trans. Antennas Propag.*, vol. 51, no. 8, pp. 1690–1705, Aug. 2003.
[11] P. Kosmas and C. M. Rappaport, "FDTD-based time reversal for microwave breast cancer detection-localization in three dimensions," *IEEE Trans. Microw. Theory Techn.*, vol. 54, no. 4, pp. 1921–1927, Jun. 2006.
[12] S. K. Davis, H. Tandradinata, S. C. Hagness, and B. D. V. Veen, "Ultrawideband microwave breast cancer detection: A detection-theoretic approach using the generalized likelihood ratio test," *IEEE Trans. Biomed. Eng.*, vol. 52, no. 7, pp. 1237–1250, Jul. 2005.
[13] Y. Xie, B. Guo, L. Xu, J. Li, and P. Stoica, "Multistatic adaptive microwave imaging for early breast cancer detection," *IEEE Trans. Biomed. Eng.*, vol. 53, no. 8, pp. 1647–1657, Aug. 2006.
[14] H. B. Lim, N. T. T. Nhung, E.-P. Li, and N. D. Thang, "Confocal microwave imaging for breast cancer detection: Delay-multiply-and-sum image reconstruction algorithm," *IEEE Trans. Biomed. Eng.*, vol. 55, no. 6, pp. 1697–1704, Jun. 2008.
[15] S. Harmer, S. Cole, N. Bowring, N. Rezgui, and D. Andrews, "On body concealed weapon detection using a phased array," *Prog. Electromagn. Res. B*, vol. 124, pp. 187–210, 2012.

[16] D. M. Sheen, D. L. McMakin, and T. E. Hall, "Three-dimensional millimeter-wave imaging for concealed weapon detection," *IEEE Trans. Microw. Theory Techn.*, vol. 49, no. 9, pp. 1581–1592, Sep. 2001.

[17] X. Zhuge and A. G. Yarovoy, "A sparse aperture MIMO-SAR-based UWB imaging system for concealed weapon detection," *IEEE Trans. Geosci. Remote Sens.*, vol. 49, no. 1, pp. 509–518, Jan. 2011.

[18] J. Eichenberger, E. Yetisir, and N. Ghalichechian, "High-gain antipodal vivaldi antenna with pseudoelement and notched tapered slot operating at (2.5 to 57) GHz," *IEEE Trans. Antennas Propag.*, vol. 67, no. 7, pp. 4357–4366, Jul. 2019.

[19] M. Amiri, F. Tofigh, A. Ghafoorzadeh-Yazdi, and M. Abolhasan, "Exponential antipodal vivaldi antenna with exponential dielectric lens," *IEEE Antennas Wireless Propag. Lett.*, vol. 16, pp. 1792–1795, 2017.

[20] Y. Yao, X. Cheng, C. Wang, J. Yu, and X. Chen, "Wideband circularly polarized antipodal curvedly tapered slot antenna array for 5G applications," *IEEE J. Sel. Areas Commun.*, vol. 35, no. 7, pp. 1539–1549, Jul. 2017.

[21] S. Pandit, A. Mohan, and P. Ray, "Metamaterial-inspired low-profile high-gain slot antenna," *Microw. Opt. Technol. Lett.*, vol. 61, no. 9, pp. 2068–2073, Sep. 2019.

[22] J. Jin, Z. Cheng, J. Chen, T. Zhou, C. Wu, and C. Xu, "Reconfigurable terahertz Vivaldi antenna based on a hybrid graphene-metal structure," *Int. J. RF Microw. Comput.-Aided Eng.*, vol. 30, Feb. 2020, Art. no. e22175.

[23] A. Delphine, M. R. Hamid, N. Seman, and M. Himdi, "Broadband cloverleaf Vivaldi antenna with beam tilt characteristics," *Int. J. RF Microw. Comput.-Aided Eng.*, vol. 30, May 2020, Art. no. e22158.

[24] Z. Wang, M. Guo, X. Zhao, L. Guo, Z. Yang, and L. Chen, "Metamaterial slabs enhanced modified antipodal Vivaldi antenna;," *Int. J. RF Microw. Comput.-Aided Eng.*, vol.'31, May 2021, Art. no. e22671.

[25] X. Huang, J. Cao, W. Zhong, and X. Jin, "High gain antipodal Vivaldi antenna with novel V-shaped air-slot," *Int. J. RF Microw. Comput.-Aided Eng.*, vol. 31, no. 11, Nov. 2021, Art. no. e22818, doi: 10.1002/mmce.22818.

[26] A. Ghosh, D. Chakravarty, and A. Chakrabarty, "Dielectric loaded directive Vivaldi antenna considering dispersion in near and far field," *Int. J. RF Microw. Comput.-Aided Eng.*, vol. 31, May 2021, Art. no. e22677.

[27] H. Cheng, L. Hua, Y. Wang, H. Yang, and T. Lu, "Design of high gain Vivaldi antenna with a compound optical lens inspired by metamaterials," *Int. J. RF Microw. Comput.-Aided Eng.*, vol. 31, no. 4, Apr. 2021, Art. no. e22570, doi: 10.1002/mmce.22570.

[28] P. Mahouti, A. Kızılay, O. Tari, A. Belen, and M. A. Belen, "Design optimization of ultra wide band vivaldi antenna using artificial intelligence," in *Proc. Int. Appl. Comput. Electromagn. Soc. Symp. (ACES)*, May 2021, pp. 1–4.

[29] E. C. Fear, X. Li, S. C. Hagness, and M. A. Stuchly, "Confocal microwave imaging for breast cancer detection: Localization of tumors in three dimensions," *IEEE Trans. Biomed. Eng.*, vol. 49, no. 8, pp. 812–822, Aug. 2002.

[30] A. O. Asok and S. Dey, "High gain elliptically tapered antipodal Vivaldi antenna with tooth shaped dielectric lens," in *Proc. Int. Symp. Antennas Propag. (APSYM)*, Dec. 2020, pp. 11–14.

[31] D. Oloumi, K. K.-M. Chan, P. Boulanger, and K. Rambabu, "SAGD process monitoring in heavy oil reservoir using UWB radar techniques," *IEEE Trans. Microw. Theory Techn.*, vol. 64, no. 6, pp. 1884–1895, Jun. 2016.

[32] D. Oloumi, M. I. Pettersson, P. Mousavi, and K. Rambabu, "Imaging of oil-well perforations using UWB synthetic aperture radar," *IEEE Trans. Geosci. Remote Sens.*, vol. 53, no. 8, pp. 4510–4520, Aug. 2015.

[33] D. Oloumi and K. Rambabu, "Metal-cased oil well inspection using near-field UWB radar imaging," *IEEE Trans. Geosci. Remote Sens.*, vol. 56, no. 10, pp. 5884–5892, Oct. 2018.

[34] F. M. Sabzevari, R. S. Winter, D. Oloumi, and K. Rambabu, "A microwave sensing and imaging method for multiphase flow metering of crude oil pipes," *IEEE J. Sel. Top. Appl. Earth Observ. Remote. Sens.*, vol. 13, pp. 1286–1297, 2020.

[35] S. Paul and M. J. Akhtar, "Novel metasurface lens-based RF sensor structure for SAR microwave imaging of layered media," *IEEE Sensors J.*, vol. 21, no. 16, pp. 17827–17837, Aug. 2021, doi: 10.1109/JSEN.2021.3084614.

[36] N. T. Kien and I.-P. Hong, "Evaluation of common building wall in see-through-wall application of ultra-wideband synthetic aperture radar," *J. Electr. Eng. Technol.*, vol. 16, no. 1, pp. 437–442, Jan. 2021.

**ATHUL O. ASOK** (Graduate Student Member, IEEE) received the B.Tech. degree in electronics and communication engineering from the National Institute of Technology, Calicut, in 2016, and the M.Tech. degree in communication engineering from the National Institute of Technology, Karnataka, in 2019. He is currently pursuing the Ph.D. degree with the Department of Electrical Engineering, Indian Institute of Technology Palakkad, India. He was a recipient of the prestigious IEEE Antennas and Propagation Society (AP-S) Fellowship 2022. He has published more than nine research papers in the area of microwave imaging. His current research interests include microwave to millimetre-wave imaging, ultra-wideband antennas, and compact antennas.

**GOKUL NATH S. J.** (Member, IEEE) received the bachelor's degree in electrical engineering from the Indian Institute of Technology Palakkad, India. He is currently an Associate Application Support Engineer at MathWorks, Hyderabad. He was a recipient of the Summer Research Fellowship Programme and AGNI Fellowship offered by the Indian Academy of Sciences and IPTIF, respectively. During the summer of 2021, he did his internship at Nanyang Technological University, Singapore as part of NTU-India Connect Programme. His current research interests include microwave imaging, its related algorithms (frequency and time domain) and UWB antennas.

**SUKOMAL DEY** (Senior Member, IEEE) received the B.Tech. degree in electronics and communication engineering from the West Bengal University of Technology, Kolkata, India, in 2006, the M.Tech. degree in mechatronics engineering from the Indian Institute of Engineering Science and Technology, Shibpur, India, in 2008, and the Ph.D. degree from the Centre for Applied Research in Electronics, Indian Institute of Technology Delhi, New Delhi, India, in July 2015.

From August 2015 to July 2016, he was a Project Scientist at the Industrial Research and Development Centre, IIT Delhi, and also worked on a collaborative research project supported by Synergy Microwave Corporation, Paterson, NJ, USA. From August 2016 to June 2018, he was a Postdoctoral Research Fellow at the Radio Frequency Microsystem Laboratory, National Tsinghua University, Taiwan. Since June 2018, he has been an Assistant Professor with the Department of Electrical Engineering, Indian Institute of Technology Palakkad, Palakkad, India. For his M.Tech. dissertation (one year), he was with the Central Electronics Engineering Research Institute, Pilani, India, in 2009. He has authored or coauthored more than 120 research articles, two state-of-the art books, two book chapters, and filed 16 patents. His research interests include electromagnetic metamaterial structures, frequency selective surfaces, microwave imaging, and microwave-integrated circuits, including antennas and RFMEMS. He was a recipient of the Postgraduate Student Award from the Institute of Smart Structure and System, Bangalore, India, in 2012, the Best Industry Relevant Ph.D. Thesis Award from the Foundation for Innovation in Technology Transfer, IIT Delhi, in 2016, the Distinction in Doctoral Research 2016 from IIT Delhi, the Postdoctoral Fellow Scholarships from the Ministry of Science and Technology, Taiwan, in 2016 and 2017, respectively, the Early Career Research Award from the Science and Engineering Research Board (SERB), Government of India, in 2019, the Smt. Ranjana Pal Memorial Award (2021) from the Institution of Electronics and Communication Engineers, and several Best Paper Awards from national and international IEEE conferences with his students. He has been inducted in the technical program committee 4 and 6 of the IEEE MTT Society.